

Full Length Article

Iron single atoms and clusters anchored on natural N-doped nanocarbon with dual reaction sites as superior Fenton-like catalysts

Xin Mao^a, Zhaoyan Deng^a, Yiming Liu^a, Haiyang Xie^a, Qian He^b, Yanjuan Zhang^a,
Zuqiang Huang^a, Huayu Hu^{a,*}, Tao Gan^{a,b,*}

^a School of Chemistry and Chemical Engineering, Guangxi University, Nanning 530004, PR China

^b Fine Chemical Industry Research Institute, School of Chemistry, Sun Yat-sen University, Guangzhou 510275, PR China



ARTICLE INFO

Keywords:

Natural N-doped nanocarbon
Fenton-like processes
Single atoms and ultra-small clusters
Dual reaction sites catalyst
Ball milling

ABSTRACT

Ultra-small metal clusters have emerged as one of the most promising alternatives to heterogeneous Fenton-like catalysts. Despite the high atom utilization and structural stability of catalysts with ultra-small clusters and single-atom sites, there is still challenging for the synthesis of these catalysts due to their facile aggregation. Herein, we successfully fabricated a catalyst (Fe-NC-900) with single-atom sites and ultra-small clusters by a ball milling method combined with subsequent pyrolysis process. Fe-NC-900 showed high efficiency and superior stability in the activation of peroxydisulfate (PMS) for catalytic oxidation of refractory organic compounds. Chemical quenching experiments, electron paramagnetic resonance (EPR), in-situ Raman spectra, and electrochemical analysis indicated that the ¹O₂ oxidation was the main non-radical pathway rather than the high-valent iron oxidation and electron transfer mechanism for the degradation of RhB in the Fe-NC-900/PMS system. This work provides useful insights into the design and synthesis of the catalysts with single atoms and ultra-small clusters for practical applications in Fenton-like catalytic processes.

1. Introduction

The Fenton-like method, as a particularly promising strategy, is the elimination of hard-to-degrade organic pollutants by free radicals to address the increasing environmental pollution and shortage of freshwater resources due to industrialization [1–4]. While in Fenton-like systems, peroxydisulfate (PMS) is a strongly reactive oxidant due to its asymmetric structure, which is more easily activated over a wide pH range compared to other oxidants such as ozone (O₃), H₂O₂, and persulfate (PDS) [5–7]. In recent years, various PMS activation methods such as alkali, ultraviolet (UV) light, ultrasound, and metal compounds have been extensively investigated [8–11]. Among them, heterogeneous Fenton-based catalysts with the advantages of easy separation, low-cost, low toxicity, and good environmental compatibility have been widely used in the activation of PMS. However, low catalytic performance, iron atom aggregation, and iron leaching restrict their development [12–15]. In addition, Duan et al. [16–19] have made great progress in the activation of PMS by nitrogen-doped carbon materials through free radical and non-free radical reaction processes, but there are still the problems of insufficient oxidation performance of oxidants and poor stability in

both free radical and non-free radical pathways, which greatly limited their application in Fenton-like system. Therefore, the design and synthesis of Fenton-like catalysts with excellent stability and activity to activate PMS is essential to realize their practical applications.

In the reaction dominated by the radical oxidation process, most of the oxygen-containing radicals generated by PMS activation have a very short half-life (1 μs for ·OH, 30–40 μs for SO₄^{·-}) [3,20]. To maximize the catalytic performance, it is highly desirable to minimize the migration distance of the active radicals to the target organic molecules [21–23]. Yang et al. [24] prepared Fe-N_x site atomically dispersed Fe-SA-N/C catalysts for efficient catalytic oxidation of refractory bisphenol A (BPA) by activating PMS [20], which showed that BPA was adsorbed by pyrrolic-N near the iron-nitrogen bond; simultaneously, the PMS was activated by the active center of the iron-nitrogen bond to generate free radicals, thus effectively improving the utilization rate of free radicals generated by PMS. To this end, the construction of the catalysts with dual reactive sites that can independently recognize/activate the respective target functional groups of the substrate, achieving the generation of active radicals on the catalytic sites for pollutant removal and the adsorption of the target pollutant on the adsorption sites to

* Corresponding authors at: School of Chemistry and Chemical Engineering, Guangxi University, Nanning 530004, PR China (T. Gan).
E-mail addresses: yuhuhu@163.com (H. Hu), gant@gxu.edu.cn (T. Gan).

effectively improve the radicals utilization [21,25–27]. Therefore, it is desired to synthesize a N-doped carbon-based Fenton-like catalyst with coexistence of active and adsorption sites to improve the radicals utilization of PMS.

Recently, the catalysts with single atoms and ultra-small clusters have been used to activate PMS due to their superior performance and high atom-utilization efficiency [12,28–31]. For instance, Li et al. [5] prepared catalyst (FeCN₅) with Fe single atoms and ultra-small clusters for catalytic degradation of methylene blue (MB) by co-precipitation method. The experimental results showed that the active sites were sub-nanoclusters and single atoms acting synergistically, and the degradation rate of MB was 98.9% in 10 min, and the degradation rate of MB was still up to 86.8% after 5 cycles, showing excellent stability and catalytic performance. However, the preparation methods of those catalysts with single atoms and ultra-small clusters still suffer from cumbersome preparation processes (e.g., co-precipitation and hydrothermal carbonization) [32–34], and the precursors are generally expensive and non-renewable (e.g., carbon nanotubes, formamide, polypyrrole, etc.) [29,35], which seriously affect the economic feasibility of these catalyst materials [36,37]. Currently, soybean residue, a by-product in the production process of soy milk or tofu (every 10 kg of soybean can produce about 7 kg of dry soybean residue), is rich in protein and carbohydrates. The protein and carbohydrates may be attractive precursors for the direct production of N-doped carbons [38]. In addition, the natural advantage of uniform dispersion of organic matter (protein) in biomass cells facilitates the generation of atomically dispersed active sites [39,40]. As a result, the preparation of N-doped biomass carbon using soybean residue not only meets the economic feasibility of catalyst materials, but also improves the added value and utilization of soybean residue solid waste. To solve the problems of low utilization rate of PMS radicals and economic feasibility of catalysts, it is of great practical importance to develop a simple and inexpensive method to prepare soybean residue-derived natural N-doped carbon loaded dual sites catalysts with single atoms and ultra-small clusters.

Ball milling is an effective method that does not require solvents and other additives, which is widely used in the synthesis of nanoclusters catalysts, even single-atom catalysts [41–43]. Therefore, we prepared soybean residue-derived nanocarbon anchored dual-site catalysts (Fe-NC-900) with Fe single atoms and ultra-small clusters for the efficient catalytic oxidation of Rhodamine B (RhB) by the activation of PMS using a ball milling method combined with subsequent pyrolysis process. The structure of the catalyst was characterized by a combination of aberration corrected high-angle annular dark-field scanning transmission electron microscopy (AC HAADF-STEM) and X-ray absorption spectroscopy (XAS). Moreover, electron paramagnetic resonance (EPR) and free radical quenching experiments confirmed that the single linear state oxygen generated by PMS activation and liquid chromatography-mass spectrometry (LC-MS) was performed to analyze the catalytic degradation mechanism. This study aims to reveal in detail the main active sites of the catalysts with single atoms and ultra-small clusters, as well as their efficient heterogeneous catalytic mechanism, which has superior potential for environmental remediation.

2. Materials and methods

2.1. Materials

Soybean residue was purchased from the commercial market. Iron (II) phthalocyanine (FePc, ≥97%), Rhodamine B (RhB, 95%), congo red (CR, 99%), tetracycline HCl (TC, 95%), PMS (KHSO₅•KHSO₄•K₂SO₄, 42% KHSO₅), *tert*-butanol (TBA, 99.5%), methyl alcohol (Me-OH, 99.9%), 1,4-benzoquinone (BQ, 99%), furfuryl alcohol (FFA, 99%), 5,5-dimethyl-1-pyrroline N-oxide (DMPO, 97%), 2,2,6,6-tetramethyl-1-piperidinyloxy (TEMP, 98%), dimethylsulfoxide (DMSO ≥ 99.9%), and other chemical reagents were used without further purification and obtained from Aladdin Co., Ltd., China.

2.2. Catalyst preparation

The N-codoped nanocarbon was prepared in a tube furnace. The soybean residue was heated at designated temperature (i.e. 900 °C) at a heating rate of 3 °C min⁻¹ under nitrogen atmosphere for 2 h. Then, the obtained roasted black solid substances were pickled with 2 M HCl for 12 h to remove calcium species, neutralized with a large amount of distilled water, and dried in an oven at 60 °C. By changing the final heat treatment temperature (750, 900, and 1000 °C), different N-codoped nanocarbons were obtained (i.e. NC-T, where T represents the final heat treatment temperature). Fe-NC-750, Fe-NC-900, and Fe-NC-1000 catalysts were prepared in a planetary ball mill. 5.0 g of NC-T material, 2.1 g of FePc, and 2.5 g of KHCO₃ were added in a jar for ball milling process. The mixture was milled at room temperature for 10.0 h under 300 rpm, and the obtained samples were roasted at 750, 900, and 1000 °C under nitrogen atmosphere for 2 h with a heating rate of 3 °C min⁻¹, respectively. Afterwards, the as-obtained black powders were treated with 2 M HCl at 90 °C for 24 h, washed with extensive deionized water, and dried in an oven at 60 °C. Finally, the Fe-NC-750, Fe-NC-900, and Fe-NC-1000 catalysts were obtained. The control sample (NC-900) was synthesized by the same conditions except not adding FePc.

2.3. Characterization

X-ray diffraction patterns of the samples were determined by X-ray diffractometer (XRD, Rigaku D/MAX 2500V, Cu Kα, λ = 1.542 Å). The morphology of the prepared samples was analyzed using 300 KV filed emission transmission electron microscope (HRTEM, FEI TECNAI G2 F30, USA) and high-angle annular case field scanning projected electron-microscopy with spherical aberration correction (AC HAADF-STEM, JEM-ARM200F, Japan). The specific surface area was measured by Brunauer-Emmett-Teller (BET) method. Elemental analysis (EA) was performed on a VarioELIII analyzer (Elementar, Germany). The iron content of the samples was determined by inductively coupled plasma optical emission spectrometry (ICP-OES, PerkinElmer 8300, USA). Electron paramagnetic resonance (EPR) spectroscopy was performed using a paramagnetic resonance spectrometer (Bruker EMXplus, Germany). The valence state and surface composition of the samples were obtained by Raman spectroscopy (Raman, LabRam HR Evolution, USA) and X-ray photoelectron spectrometer (XPS, Thermo ESCALAB 250XI, USA). The degradation products of RhB were determined by Liquid chromatograph-mass spectrometer (LC-MS, ORBITRAP ELITE, USA). Total organic carbon (TOC) analysis was also used to determine the degradation efficiency of RhB. Fe K-edge X-ray adsorption fine structure (XAFS) spectra were detected in the Shanghai synchrotron irradiation facility.

2.4. Catalytic activity test

RhB solution (100 mg L⁻¹) was added to a 100 mL conical flask, and the initial solution pH was adjusted to 3.0 with 2 M HCl. The temperature was maintained at 30 °C using a water bath in a constant temperature shaker (170 r min⁻¹). In the experiments, 40 mg of catalyst and 30 mg of PMS were added to 50 mL of RhB solution, and 1 mL was sampled at various predetermined times. The catalyst was filtered out using a 0.22 μm nylon syringe and the full wavelength was displayed using a UV-Vis spectrometer (2802S UV/VIS Spectrometer) in the range 400–1100 nm, wavelength the maximum permissible error: ±0.8 nm, measured at its maximum absorption wavelength of 554 nm. Each test was duplicated three times. The catalyst was thoroughly washed with a large amount of deionized water as well as ethanol each time during the cyclic experiments, and the amount of iron leached from the catalyst was determined by ICP-OES. The reaction rate was calculated by the proposed first-order kinetic model (Eq. (1)) and the adsorption rate was calculated by Eq. (2).

$$\ln(C_0/C_t) = kt \quad (1)$$

$$R \% = 100 \times (C_0 - C_e) / C_0 \quad (2)$$

where C_0 is the original concentration of the pollutant, C_t is the concentration at a point time in the degradation process, C_e is the concentration at equilibrium of the catalyst, and k is the reaction rate constant.

3. Results and discussion

3.1. Characterization of Fe-NC-900 catalyst

The preparation process of Fe-NC catalysts using soybean residue carbonized material (N-doped carbon) as the support is shown in Fig. 1. The N-doped carbon was mixed with FePc and potassium bicarbonate in a certain ratio (2:1:0.85), and then the mixture was completely ball milled in a planetary ball mill. After that, the samples were roasted at 750, 900, and 1000 °C under N₂ atmosphere, then acid etched and dried to obtain Fe-NC-750, Fe-NC-900, and Fe-NC-1000 (the yield was about 58.8%), respectively. TEM and STEM images (Fig. 2a and b) showed that there were no obvious iron nanoparticles, demonstrating the homogeneity of the dispersion of Fe metal. The Fe single atoms (yellow circles) and clusters (red circles) were detected by AC HAADF-STEM (Fig. 2c and f). A number of ultra-small Fe clusters were uniformly distributed in the N-doped carbon support. Further examination (Fig. 2f) showed that both single-atom Fe sites and ultra-small clusters were uniformly dispersed in Fe-NC-900. EDX mapping images (Fig. 2d and e) also confirmed that N, C, O and Fe elements were uniformly distributed on carbon support. The XRD patterns (Fig. 3a) showed that only two broad diffraction peaks were clearly observed at 25° and 44°, corresponding to the (002) and (101) faces of graphitic carbon [33]. It is noted that no diffraction peaks corresponding to Fe or FeO_x were detected, implying that the size of Fe cluster was small enough [44], which was in agreement with the TEM/STEM results. In addition, the N-doped nanocarbons structure of Fe-NC-900 was characterized by Raman measurement (Fig. 3b). The intensity ratio of D and G bands (I_D/I_G) in the samples indicated that the I_D/I_G value of the Fe-NC-900 (1.03) was lower than that of NC-900 (1.08), i.e., the degree of graphitization and electrical conductivity was higher [27]. From the N₂ adsorption/desorption isotherm curves of the samples in Fig. S1 in the Supporting Information. The BET surface area (Table S1) of NC-900 (595.3 m² g⁻¹) was larger than those of Fe-NC-750 (418.2 m² g⁻¹), Fe-NC-900 (411.3 m² g⁻¹), and Fe-NC-1000 (401.2 m² g⁻¹), probably causing by the Fe species entering into the pores, which decreased the specific surface area of Fe-NC catalysts.

The key to determine the catalytic performance of catalysts is the chemical state of the metal-Fe clusters, as well as the Fe single atoms, and their environment. Therefore, XPS analysis was performed to collect

high-resolution N 1s XPS spectra of the as-prepared catalysts to quantify the type and content of nitrogen doping. As displayed in Fig. 3c, the deconvolution yielded three peaks with binding energies of 398.4, 399.8, and 401.1 eV, attributed to pyridinic-N, pyrrolic-N, and graphite-N, respectively [45,46]. Moreover, after the doping of Fe element into the Fe-NC catalysts, the appearance of a new peak (399.0 eV) could be assigned to the metal-ligated M–N_x fraction in the three catalysts, demonstrating the presence of abundant Fe–N_x active sites [47]. Among them, the Fe-NC-900 had the highest contents of both Fe–N_x and pyrrolic-N (Table S1), causing the higher catalytic activity in the Fenton-like reaction. Furthermore, the content of pyrrolic-N of Fe-NC catalysts gradually increased with the increase of roasting temperature, as shown in Fig. 3d [48]. Previous studies have shown that the enhancement of pyrrolic-N is positively correlated to the adsorption activity of carbon-based catalysts, resulting in significant Fenton-like catalytic activity. In addition, Fe 2p_{1/2} and 2p_{3/2} of the three as-prepared samples corresponded to the peaks at 720.6 and 707.1 eV (Fig. S2a), respectively, which demonstrated the presence of Fe³⁺ and Fe²⁺ in the catalysts. The C 1s spectrum of Fe-NC-900 (Fig. S2b) exhibited three peaks at 284.5, 285.4, and 288.4 eV, attributed to C–C, C–N, and C–C=O, respectively. Furthermore, the peaks belonging to O 1s spectrum of C–C=O and O–H appeared at 531.7 and 532.5 eV (Fig. S2c), respectively [49]. The presence of C–C=O group in Fe-NC-900 was more favorable the generation of ¹O₂, which activated the PMS owing to the interaction of C–C=O with PMS. Moreover, ICP-OES analysis showed that the Fe contents (Table S1) of Fe-NC-750, Fe-NC-900, and Fe-NC-1000 were 0.32, 0.41, and 0.34 wt%, respectively. The P, S, K, and Ca contents of soybean residue and Fe-NC-900 were also obtained from ICP-OES, as shown in Table S2. The contents of S, P, K, and Ca for soybean residue were 0.03, 0.06, 0.21, and 0.10 wt%, respectively. The contents of S, P, K, and Ca for Fe-NC-900 were 0.01, 0.02, 0.003, and 0.0002 wt%, respectively.

As shown in Fig. 4a, a small leading edge peak at 7114.8 eV in the Fe K-edge XANES spectrum of Fe-NC-900 indicated the presence of Fe(II) and Fe(III), which was consistent with the XPS results [50]. Arising from the 1s → 4p_z leap in the ligand-to-metal transfer, it is considered as a square of the Fourier transform altered-weighted EXAFS spectrum planar Fe–N_x unitary (D_{4h} symmetry) fingerprinting [20]. As illustrated in Fig. 4b, compared with the standard samples of Fe foil, FeO, Fe₂O₃, and Fe₃O₄, no prominent peak (~2.10 Å) at the Fe–Fe coordination position was discovered in Fe-NC-900, which might be ascribed to that the metal loading of the iron clusters was low in Fe-NC-900. In addition, the N-doped carbon-encapsulated metallic iron species were formed around the isolated Fe–N sites at high temperatures, resulting in very weak Fe–Fe peaks [51,52]. The peak of Fe-NC-900 at ~1.56 Å (phase uncorrected distance) indicated that the Fe–N bond distance of the catalyst was longer than the Fe–O bond (~1.4 Å) in FeO, Fe₂O₃, and Fe₃O₄. Furthermore, no large high-shell peaks (in the range of 2–3 Å) were present [36], which demonstrated a large number of Fe species atom dispersion in the Fe-NC-900. As displayed in Fig. 4c–g, wavelet transform contour plot of Fe foil showed Fe–Fe signal intensity maxima at about 7.8 Å⁻¹; wavelet transform contour plots of FeO, Fe₂O₃, and Fe₃O₄ as well as Fe₂O₃ showed Fe–O at a maximum at 4.4 Å⁻¹; while wavelet transform contour plot of Fe-NC-900 showed Fe–N signal intensity maxima at about 5 Å⁻¹, further demonstrating the atomic dispersion of the Fe atoms. Furthermore, the oscillation curves of experiment and fitting data are displayed in Fig. S3, and the EXAFS fitting parameters are shown in Table S3. The FT-EXAFS fitting results revealed a coordination number of 4.3, and an average Fe–N bond length of $d_{\text{Fe-N}}$ was about 2.01 Å.

Thus, the above characterizations confirmed that all Fe sites in the Fe-NC-900 were highly dispersed ultra-small clusters and single atoms, mainly consisting of Fe–N_x and Fe–Fe bonds, which demonstrated the successful preparation of Fe-NC-900 catalysts.

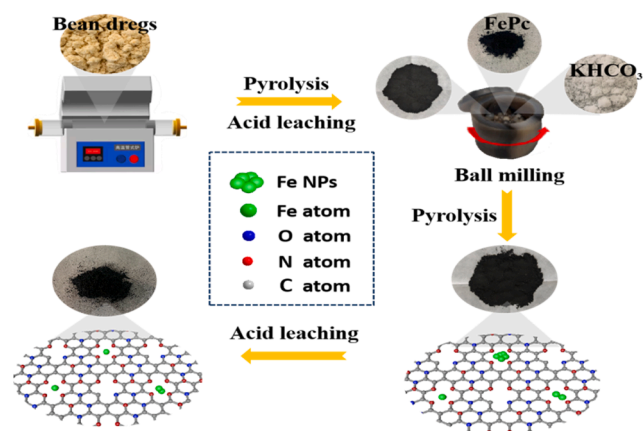


Fig. 1. Schematic illustration of preparation process of Fe-NC catalysts by ball milling method combined with subsequent pyrolysis process.

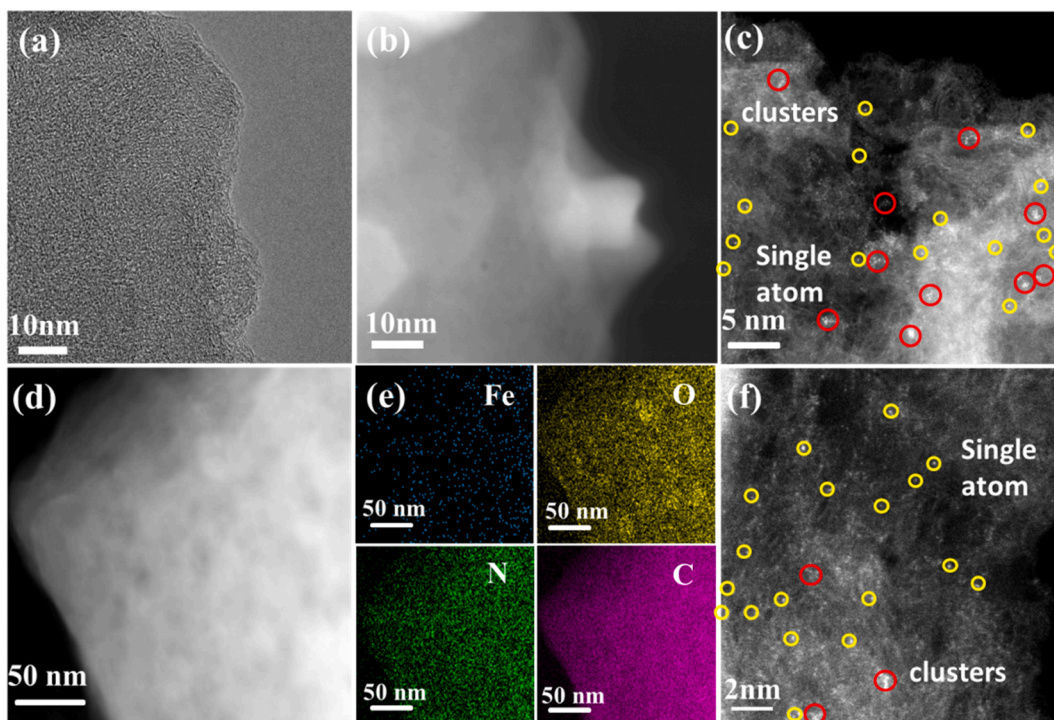


Fig. 2. Structural characterization of Fe-NC-900. (a) TEM image; (b) STEM image; (c,f) HAADF-STEM images; (d,e) EDX mappings.

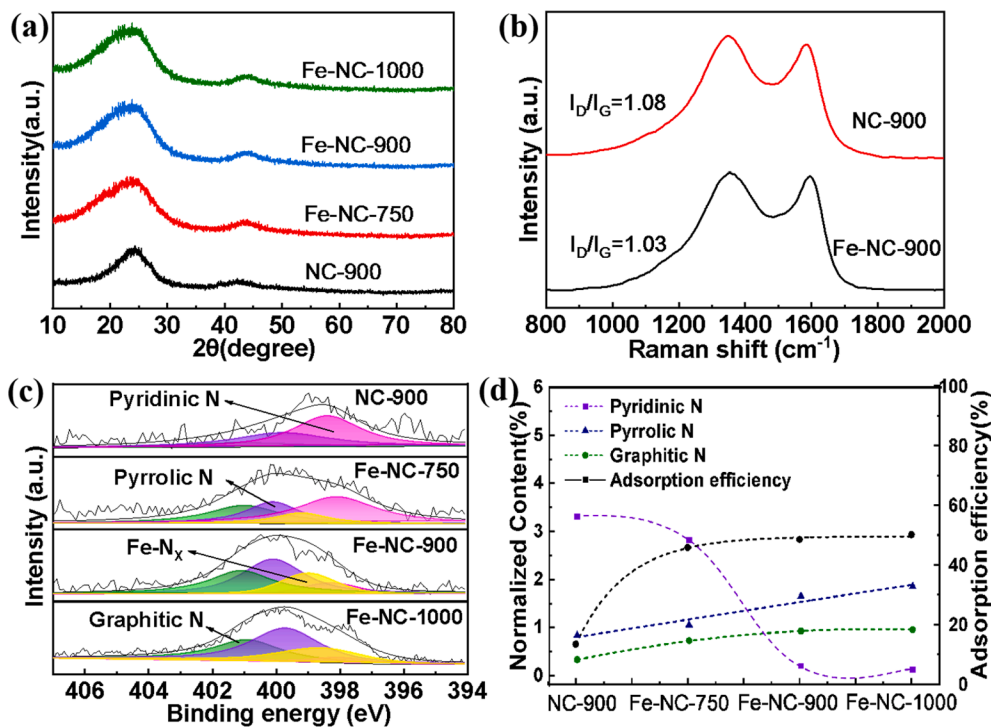


Fig. 3. (a) XRD patterns of NC-900, Fe-NC-750, Fe-NC-900, and Fe-NC-1000; (b) Raman spectra of NC-900 and Fe-NC-900; (c) N 1s core level XPS spectra of NC-900, Fe-NC-750, Fe-NC-900, and Fe-NC-1000; (d) Relationship of RhB adsorption efficiency and the content of graphitic-N, pyrrolic-N, and pyridinic-N.

3.2. Catalytic activity of Fe-NC catalysts

Fig. 5a shows the degradation of RhB in different reaction systems. It is noteworthy that the removal efficiencies of RhB in NC-900 and NC-900/PMS systems were only 16.9% and 30.1% in 10 min, respectively, indicating that NC-900 could slightly enhance the activation rate of PMS. The removal efficiencies of RhB in 10 min were 75.3% and 81.2%

for Fe-NC-750/PMS and Fe-NC-1000/PMS systems, respectively, yet the pollutants could not be completely degraded. Encouragingly, the Fe-NC-900/PMS system achieved a 99.5% RhB removal rate in 10 min, indicating that the Fe ultra-small clusters and single atoms were regarded as the primary catalytic active-sites for the degradation of RhB. To further investigate the catalytic activity of Fe-NC-900, the RhB degradation kinetics was also described by using a pseudo-first-order model. As

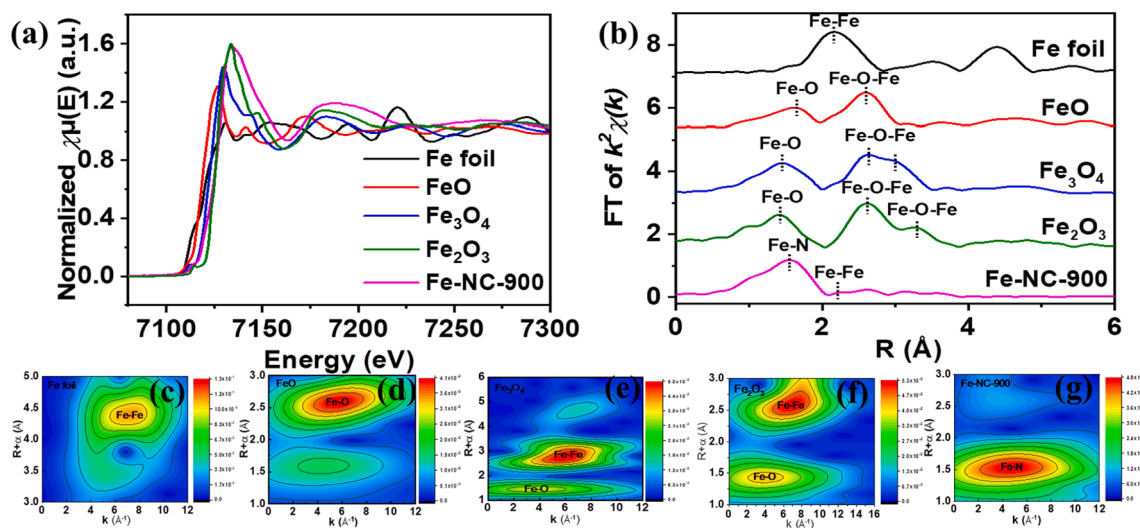


Fig. 4. Structural characterizations of Fe-NC-900 catalyst by XAS. (a) Normalized Fe K-edge XANES spectra, (b) corresponding EXAFS fitting curves, and (c-g) Fe K-edge wavelet transformed (WT) EXAFS for Fe foil, FeO, Fe₃O₄, Fe₂O₃, and Fe-NC-900.

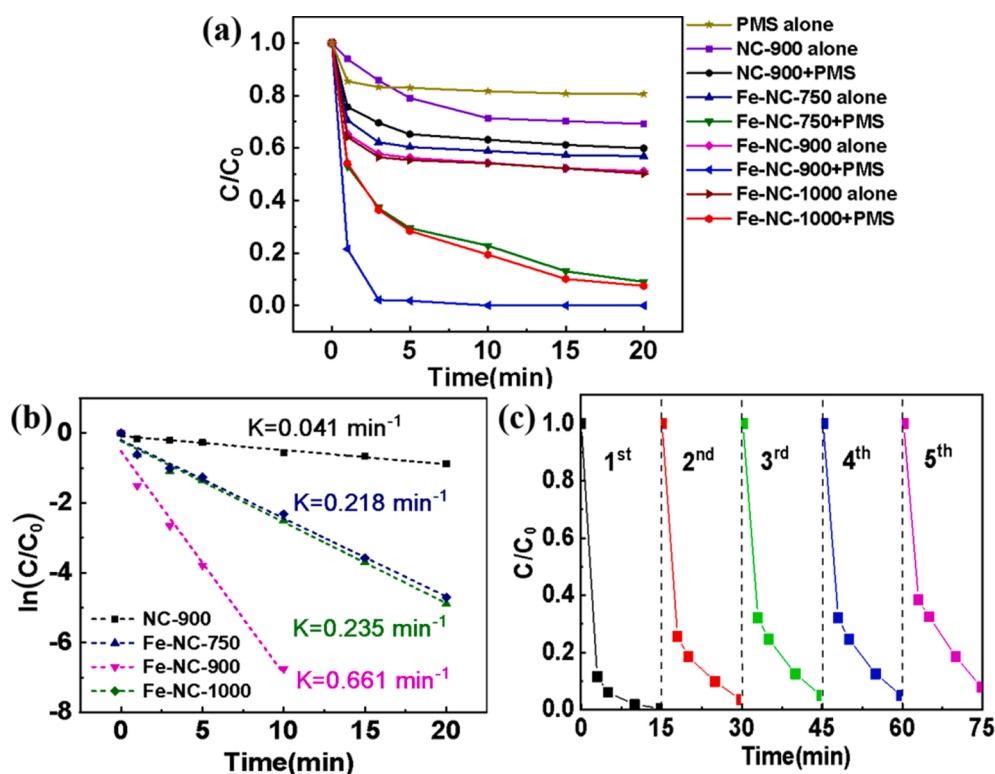


Fig. 5. (a) Adsorption and degradation of RhB by PMS activation over the catalysts; (b) Proposed first-order kinetic fitting of RhB degradation by PMS over the catalysts; (c) Continuous operation to investigate the evolution of Fe-NC-900 catalytic activity. (Conditions: T = 30 °C, [catalyst]₀ = 0.8 g L⁻¹, [pollutants]₀ = 100 mg L⁻¹, [PMS]₀ = 0.6 g L⁻¹, and pH = 3.0.)

shown in Fig. 5b, the rate constant (k) of Fe-NC-900 (0.661 min⁻¹) was 3, 2.8, and 16 times higher than those of Fe-NC-750 (0.218 min⁻¹), Fe-NC-1000 (0.235 min⁻¹), and NC-900 (0.041 min⁻¹), respectively, which suggested the superior catalytic performance of Fe-NC-900. In addition, the TOC removal rate of RhB was 45.5% after 30 min in Fe-NC-900/PMS system (Fig. S4a).

Reusability was also one of the crucial indicators to evaluate the performance of the catalysts. As exhibited in Fig. 5c, after five replicate experiments, the degradation rate of RhB only decreased by 8.7%, indicating the excellent stability of Fe-NC-900. We examined the high-

resolution N 1s XPS spectra of the Fe-NC-900 catalyst before and after reaction. The RhB removal efficiency gradually decreased to 90.8% after the reaction while the pyrrolic-N content also decreased (Fig. S5a). The ICP-OES results showed that the loss of Fe after 5 runs accounted for about 7% (Table S1), indicating that the gradual decrease in Fe-NC-900 activity may be related to the leaching of Fe species. Moreover, the HETEM images (Fig. S6a-c and f), EDX mappings (Fig. S6d-e), and XRD (Fig. S5b) patterns of Fe-NC-900 before and after reaction were essentially unchanged, which further confirmed that the structure of Fe-NC-900 catalyst was stable. Surprisingly, Fe-NC-900 exhibited excellent

catalytic performance for the degradation of CR and TC under similar conditions (Fig. S4b). As shown in Table S4, Fe-NC-900 also had significant advantages over other catalysts in terms of catalytic performance. In summary, Fe-NC-900/PMS system showed excellent catalytic performance in different organic wastewater treatment, which is highly promising for environmental treatment.

3.3. Identification of reactive species and degradation mechanism

The reactive radicals generated during PMS activation were determined by free radical quenching experiments. Usually, as a rule of thumb, TBA ($\cdot\text{OH}$ radical scavenger) and Me-OH were used for the capture of $\text{SO}_4^{\cdot-}$ and $\cdot\text{OH}$ based radicals. As shown in Fig. 6a, the addition of 0.5 M TBA or Me-OH did not significantly change the catalytic performance, confirming that $\text{SO}_4^{\cdot-}$ and $\cdot\text{OH}$ based radicals had no effect on the catalytic process [37]. 5,5-Dimethyl-1-pyrroline-N-oxide (DMPO) spin capture EPR experimental measurements were used to confirm the presence of $\text{SO}_4^{\cdot-}$ and $\cdot\text{OH}$ based radicals. Fig. 6b shows the absence of significant peaks for the DMPO- $\text{SO}_4^{\cdot-}$ and DMPO- $\cdot\text{OH}$ adducts, further indicating that $\text{SO}_4^{\cdot-}$ and $\cdot\text{OH}$ based radicals were not involved in the degradation of Fe-NC-900/PMS system. Besides, the addition of BQ in the Fe-NC-900/PMS system had little effect on the $\text{O}_2^{\cdot-}$ capture effect, which proved that $\text{O}_2^{\cdot-}$ did not play a major role in the Fe-NC-900/PMS system.

Notably, confirming the oxidation of DMPO to generate DMPOX, which suggested that DMPO was directly oxidized rather than attacked by free radicals in the Fe-NC-900/PMS system, and the DMPOX was generated by the reaction of $^1\text{O}_2$ with DMPO [53]. Therefore, the catalytic reaction of Fe-NC-900/PMS system was carried out by non-radical mechanism.

Currently, non-radical oxidation dominated by high-valent iron-oxygen complexes, electron transfer as well as $^1\text{O}_2$ were found in large numbers in PMS oxidative degradation systems. Moreover, in the EPR spectra, the TEMP as a spin-capture agent demonstrated the presence of $^1\text{O}_2$ [3,54]. As shown in Fig. 6b, the TEMP adduct detected a triple

signal of equal intensity, indicating the generation of $^1\text{O}_2$. However, previous studies suggested that electron transfer can also form TEMPO. Thus, the FFA was used as a trapping agent for $^1\text{O}_2$ in the Fe-NC-900/PMS system. The addition of FFA to the catalytic system resulted in a decrease of the degradation efficiency of RhB from 99.5% to 30% (Fig. 6a). Moreover, while RhB degradation was slightly affected by the introduction of 5 mM DMSO in the Fe-NC-900/PMS system (Fig. 6c), the degradation rate decreased from 99.5% to 98.1%. With the addition of different amounts of DMSO, the RhB degradation rate decreased to 93%, implying the involvement of highly valent iron-oxygen species in the Fe-NC-900/PMS system, however, which did not play a major role for RhB degradation [55]. The role of non-radical electron transfer mechanisms in the catalytic process was investigated by in-situ Raman spectroscopy experiments and electrochemical measurements. As shown in Fig. S7a, a new peak appeared around 830 cm^{-1} after the addition of Fe-NC-900 to the PMS solution, which is supposed to be due to the formation of activated perovskite species (PMS*). Fig. S7b shows that the current density increased after the addition of RhB and PMS, indicating that there was a current flow from RhB to the sub-stable reaction complex between PMS and Fe-NC-900 [56]. Moreover, a smaller semicircle diameter was observed in the electrochemical impedance spectrum (EIS). The charge transfer resistance of the Fe-NC-900 + PMS + RhB system was reduced compared to Fe-NC-900 alone (Fig. S7c). These results further confirmed the minor role of the electron transfer-dominated nonradical oxidation pathway in the Fe-NC-900/PMS system. Based on these results, for this non-radical pathway, $^1\text{O}_2$ oxidation was the main non-radical pathway rather than the high-valent iron oxidation and electron transfer mechanism for the degradation of RhB in the Fe-NC-900/PMS system.

The UV-Vis absorption spectra (Fig. 6d) of the Fe-NC/PMS system showed that the absorption peak of RhB at 554 nm almost completely disappeared after 10 min, which was also consistent with the trend of the decolorization of the solution, proving that the degradation of RhB was almost complete. Furthermore, a blue shift of the maximum absorption peak of RhB could be clearly observed, which was caused by the

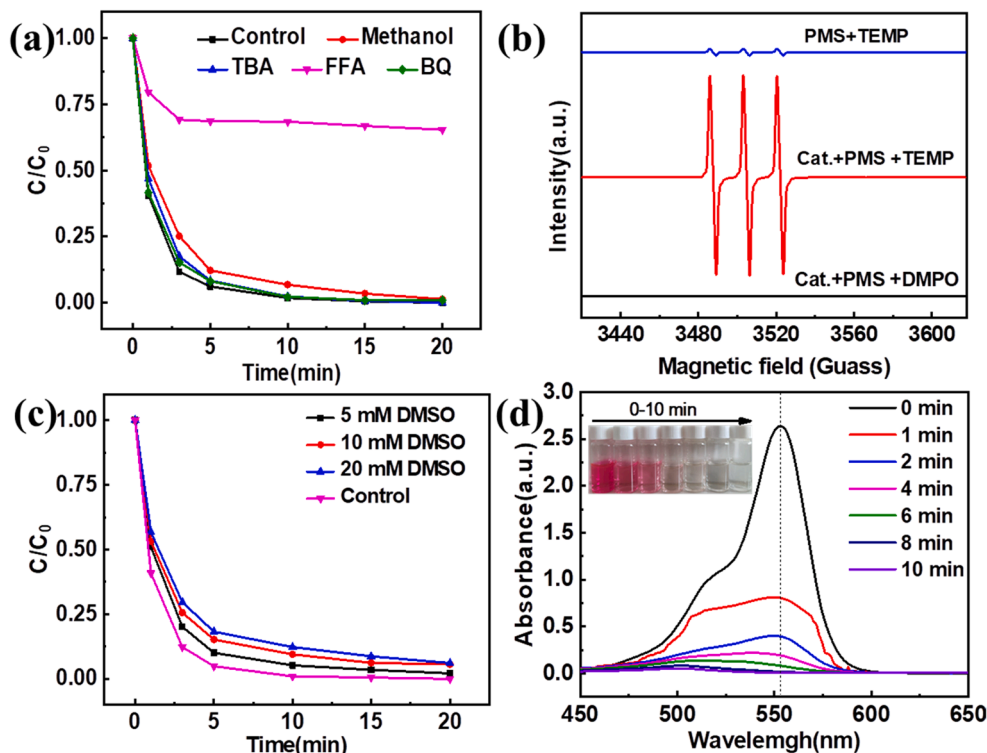


Fig. 6. (a,c) RhB degradation in the presence of various quenching agents. (b) EPR spectra obtained with DMPO and TEMP as spin-trapping agents. (d) UV-Vis spectra of RhB in Fe-NC-900/PMS system. (Conditions: [catalyst] $_0 = 0.8\text{ g L}^{-1}$, [RhB] $_0 = 100\text{ mg L}^{-1}$, [PMS] $_0 = 0.6\text{ g L}^{-1}$, and pH = 3.0.)

shedding of ethyl groups from the molecule during the catalytic degradation of RhB.

The degradation process of RhB molecules was further determined in the Fe-NC-900/PMS system with an initial pH of 3.0, initial RhB concentration of 100 mg L⁻¹, and Fe-NC-900 dosage of 0.8 g L⁻¹, and the intermediates in aqueous solution after 0, 5, and 10 min of the reaction were analyzed by LC-MS. When the catalytic system lasted for 10 min, the color of the reaction solution almost disappeared completely (Fig. 6d), suggesting that the chromium group in RhB solution was destroyed and a number of intermediate products were produced. The strong peaks at $m/z = 415, 387, 318, 274, 118, 110, 106, 94, 74,$ and 56 were observed by LC-MS (Fig. S8). The possible degradation pathways of RhB in the Fe-NC-900/PMS system and the intermediate molecules, including N-deethylation (steps 1, 2, and 3), chromophore cleavage (steps 4, 5, 7, and 9), ring opening (steps 6 and 8), and mineralization (steps 10, 11, and 12) [57], were displayed in Fig. S9. In the RhB-catalyzed system, the detected intermediates indicated that Fe-NC-900 first underwent N-deethylation reaction during the catalytic oxidation. Meanwhile, the deethylation intermediates were underwent chromophore cleavage and ring opening to yield some small molecule intermediates, such as phenol (C₆H₅-OH; $m/z = 94$), succinic acid (HOOC-CH₂-CH₂-COOH; $m/z = 118$), and propionic acid (CH₃-CH₂-COOH; $m/z = 74$). Besides, these small molecule intermediates could be mineralized to H₂O and CO₂, and -NH₂ groups could be converted to NH₄ or oxidized to NO₃. Thus, in the N-deethylation phase, the major processes were competing, including N-deethylation, chromophore cleavage, and ring opening, with the mineralization reactions occurring simultaneously [58]. Moreover, in the Fe-NC-900/PMS system, the N-deethylation reaction was completed within 5 min, while the cleavage, ring opening, and mineralization of the chromophore last longer. The degradation of RhB was mainly caused by a series of oxidation reactions. The catalytic performance of the catalyst was closely related to its redox properties, and Fe-NC-900 had reversible redox reactions of Fe²⁺ and Fe³⁺. Among them, the high valent Fe³⁺ exhibited strong oxidation, while the low valent Fe²⁺ showed reduction. In addition, Fe²⁺ can remain stable under acidic conditions and act as an adsorber and activator for oxygen in dissolved oxygen in solution. When oxygen molecules were converted into reactive oxygen species, such as O₂⁻, O⁻, and O²⁻, they were directly involved in oxidation reactions, including C-C cleavage, N-C cleavage, and C-H insertion [59]. The breakage and reorganization of these bonds were the main causes of RhB degradation reactions and color changes.

Based on the above results, we propose a possible mechanism for PMS activation toward the degradation of RhB by Fe-NC-900 catalyst. PMS tended to bind to the Fe-N_x sites and formed the PMS* intermediates. Then, the PMS intermediates were heavily activated and underwent substantial electron accumulation and depletion, which led to efficient activation of PMS to generate ¹O₂. Meanwhile, RhB was adsorbed on the pyrrolic-N sites via a “donor-acceptor” mechanism. Thus, the rapid in situ generation of ¹O₂ reacted quickly with the neighboring adsorbed RhB over catalysts with ultra-small Fe clusters and single atoms, yielding an outstanding Fenton-like catalytic performance.

4. Conclusion

In summary, we confirmed the high catalytic performance and superior stability of the as-prepared Fe-NC-900 catalyst with Fe single atoms and ultra-small clusters to activate PMS for the degradation of organic pollutant. The catalytic mechanism of Fe-NC-900 was investigated by quenching experiments, EPR, LC-MS, etc. We confirmed that the Fe-NC-900 could improve the catalytic performance by providing a large amount of Fe-N_x active sites to activate PMS, producing a large amount of ¹O₂. Meanwhile, RhB was adsorbed on the pyrrolic-N sites by the “donor-acceptor” mechanism, and eventually the in situ grown ¹O₂ reacted directly with the neighboring adsorbed RhB on the catalyst in a

rapid manner. This work has deepened our understanding of the design and catalytic mechanism of catalysts with ultra-small metal clusters and single atoms.

CRediT authorship contribution statement

Xin Mao: Methodology, Validation, Formal analysis, Investigation, Writing – review & editing. **Zhaoyan Deng:** Investigation. **Yiming Liu:** Investigation, Formal analysis. **Haiyang Xie:** Investigation. **Qian He:** Software. **Yanjuan Zhang:** Supervision. **Zuqiang Huang:** Supervision. **Huayu Hu:** Supervision, Writing – review & editing. **Tao Gan:** Methodology, Supervision, Writing – review & editing, Resources.

Declaration of Competing Interest

The authors declare that they have no known competing financial interests or personal relationships that could have appeared to influence the work reported in this paper.

Acknowledgements

The authors acknowledge the financial support from the National Natural Science Foundation of China (Nos. 22068007, 22178074 and 22008041), the Guangxi Natural Science Foundation (Nos. 2019GXNSFDA245020 and 2020GXNSFGA297001), the Guangdong Basic and Applied Basic Research Foundation (2020A15110864), the Guangdong Natural Science Foundation (2021A1515010163).

Appendix A. Supplementary data

Supplementary data to this article can be found online at <https://doi.org/10.1016/j.apsusc.2022.153625>.

References

- [1] S.S. Gupta, M. Stadler, C.A. Noser, A. Ghosh, B. Steinhoff, D. Lenoir, C.P. Horwitz, K.-W. Schramm, T.J. Collins, Rapid total destruction of chlorophenols by activated hydrogen peroxide, *Science* 296 (5566) (2002) 326–328.
- [2] M.A. Shannon, P.W. Bohn, M. Elimelech, J.G. Georgiadis, B.J. Mariñas, A. M. Mayes, Science and technology for water purification in the coming decades, *Nature* 452 (7185) (2008) 301–310.
- [3] X. Li, X. Huang, S. Xi, S. Miao, J. Ding, W. Cai, S. Liu, X. Yang, H. Yang, J. Gao, J. Wang, Y. Huang, T. Zhang, B. Liu, Single cobalt atoms anchored on porous N-doped graphene with dual reaction sites for efficient Fenton-like catalysis, *J. Am. Chem. Soc.* 140 (39) (2018) 12469–12475.
- [4] H. Zhou, J. Yang, W. Cao, C. Chen, C. Jiang, Y. Wang, Hollow meso-crystalline Mn-doped Fe₃O₄ Fenton-like catalysis for ciprofloxacin degradation: applications in water purification on wide pH range, *Appl. Surf. Sci.* 590 (2022) 153120.
- [5] B. Li, X. Cheng, R. Zou, X. Yong, C. Pang, Y. Su, Y. Zhang, Simple modulation of Fe-based single atoms/clusters catalyst with acidic microenvironment for ultrafast Fenton-like reaction, *Appl. Catal. B-Environ.* 304 (2022) 121009.
- [6] J. Wang, B. Li, Y. Li, X. Fan, F. Zhang, G. Zhang, W. Peng, Facile synthesis of atomic Fe-N-C materials and dual roles investigation of Fe-N_x sites in Fenton-like reactions, *Adv. Sci.* 8 (22) (2021) 2101824.
- [7] R. Xiao, L. He, Z. Luo, R. Spinney, Z. Wei, D.D. Dionysiou, F. Zhao, An experimental and theoretical study on the degradation of clonidine by hydroxyl and sulfate radicals, *Sci. Total. Environ.* 710 (2020) 136333.
- [8] J. Wang, S. Wang, Activation of persulfate (PS) and peroxymonosulfate (PMS) and application for the degradation of emerging contaminants, *Chem. Eng. J.* 334 (2018) 1502–1517.
- [9] F. Ghanbari, M. Moradi, Application of peroxymonosulfate and its activation methods for degradation of environmental organic pollutants: review, *Chem. Eng. J.* 310 (2017) 41–62.
- [10] S. Waclawek, H.V. Lutze, K. Grübel, V.V.T. Padil, M. Černík, D.D. Dionysiou, Chemistry of persulfates in water and wastewater treatment: a review, *Chem. Eng. J.* 330 (2017) 44–62.
- [11] J. Hou, X. He, S. Zhang, J. Yu, M. Feng, X. Li, Recent advances in cobalt-activated sulfate radical-based advanced oxidation processes for water remediation: a review, *Sci. Total. Environ.* 770 (2021) 145311.
- [12] N. Thomas, D.D. Dionysiou, S.C. Pillai, Heterogeneous Fenton catalysts: a review of recent advances, *J. Hazard. Mater.* 404 (2021) 124082.
- [13] Y. Sun, L. Silvioli, N.R. Sahaie, W. Ju, J. Li, A. Zitolo, S. Li, A. Bagger, L. Armarson, X. Wang, T. Moeller, D. Bernsmeier, J. Rossmeisl, F. Jaouen, P. Strasser, Activity-selectivity trends in the electrochemical production of hydrogen peroxide over

- single-site metal-nitrogen-carbon catalysts, *J. Am. Chem. Soc.* 141 (31) (2019) 12372–12381.
- [14] S. Zhang, Q. Fan, H. Gao, Y. Huang, X. Liu, J. Li, X. Xu, X. Wang, Formation of $\text{Fe}_3\text{O}_4/\text{MnO}_2$ ball-in-ball hollow spheres as a high performance catalyst with enhanced catalytic performances, *J. Mater. Chem. A* 4 (4) (2016) 1414–1422.
- [15] Y. Xiong, H. Li, C. Liu, L. Zheng, C. Liu, J.O. Wang, S. Liu, Y. Han, L. Gu, J. Qian, D. Wang, Single-atom Fe catalysts for Fenton-like reactions: roles of different N species, *Adv. Mater.* 34 (2022) 2110653.
- [16] X. Duan, H. Sun, Z. Shao, S. Wang, Nonradical reactions in environmental remediation processes: uncertainty and challenges, *Appl. Catal. B-Environ.* 224 (2018) 973–982.
- [17] X. Duan, H. Sun, J. Kang, Y. Wang, S. Indrawirawan, S. Wang, Insights into heterogeneous catalysis of persulfate activation on dimensional-structured nanocarbons, *ACS Catal.* 5 (8) (2015) 4629–4636.
- [18] X. Duan, Z. Ao, H. Sun, S. Indrawirawan, Y. Wang, J. Kang, F. Liang, Z.H. Zhu, S. Wang, Nitrogen-doped graphene for generation and evolution of reactive radicals by metal-free catalysis, *ACS Appl. Mater. Inter.* 7 (7) (2015) 4169–4178.
- [19] X. Duan, H. Sun, Y. Wang, J. Kang, S. Wang, N-doping-induced nonradical reaction on single-walled carbon nanotubes for catalytic phenol oxidation, *ACS Catal.* 5 (2) (2015) 553–559.
- [20] J. Yang, D. Zeng, J. Li, L. Dong, W.-J. Ong, Y. He, A highly efficient Fenton-like catalyst based on isolated diatomic Fe-Co anchored on N-doped porous carbon, *Chem. Eng. J.* 404 (2021) 126376.
- [21] H. Xu, N. Jiang, D.a. Wang, L. Wang, Y. Song, Z. Chen, J. Ma, T. Zhang, Improving PMS oxidation of organic pollutants by single cobalt atom catalyst through hybrid radical and non-radical pathways, *Appl. Catal. B-Environ.* 263 (2020) 118350.
- [22] H. Li, C. Shan, B. Pan, Fe(III)-doped $g\text{-C}_3\text{N}_4$ mediated peroxymonosulfate activation for selective degradation of phenolic compounds via high-valent iron-oxo species, *Environ. Sci. Technol.* 52 (4) (2018) 2197–2205.
- [23] J. Li, J. Li, A. Liu, J. Guo, Y. Liu, X. Jiang, W. Cen, Mechanism of over-stoichiometric oxidation of SO_2 by iron oxides modified pyridinic N-doped carbonaceous materials, *Appl. Surf. Sci.* 556 (2021) 149757.
- [24] T. Yang, S. Fan, Y. Li, Q. Zhou, Fe-N/C single-atom catalysts with high density of Fe- N_x sites toward peroxymonosulfate activation for high-efficient oxidation of bisphenol A: electron-transfer mechanism, *Chem. Eng. J.* 419 (2021) 129590.
- [25] Z. Chen, S. Pronkin, T.-P. Fellingner, K. Kailasam, G. Vilé, D. Albani, F. Krumeich, R. Leary, J. Barnard, J.M. Thomas, J. Pérez-Ramírez, M. Antonietti, D. Dontsova, Merging single-atom-dispersed silver and carbon nitride to a joint electronic system via copolymerization with silver tricyanomethanide, *ACS Nano* 10 (3) (2016) 3166–3175.
- [26] S. Hu, W. Ni, D. Yang, C. Ma, J. Zhang, J. Duan, Y. Gao, S. Zhang, Fe_3O_4 nanoparticles encapsulated in single-atom Fe-N-C towards efficient oxygen reduction reaction: effect of the micro and macro pores, *Carbon* 162 (2020) 245–255.
- [27] R. Yun, F. Zhan, N.a. Li, B. Zhang, W. Ma, L. Hong, T. Sheng, L. Du, B. Zheng, S. Liu, Liu, Fe single atoms and Fe_2O_3 clusters liberated from N-doped polyhedral carbon for chemoselective hydrogenation under mild conditions, *ACS Appl. Mater. Inter.* 12 (30) (2020) 34122–34129.
- [28] S. An, G. Zhang, T. Wang, W. Zhang, K. Li, C. Song, J.T. Miller, S. Miao, J. Wang, X. Guo, High-density ultra-small clusters and single-atom Fe sites embedded in graphitic carbon nitride ($g\text{-C}_3\text{N}_4$) for highly efficient catalytic advanced oxidation processes, *ACS Nano* 12 (9) (2018) 9441–9450.
- [29] J. Shi, Y. Zhang, Y. Zhu, M. Chen, Z. Zhang, W. Shangguan, Efficient Fe-ZSM-5 catalyst with wide active temperature window for NH_3 selective catalytic reduction of NO: synergistic effect of isolated Fe^{3+} and Fe_2O_3 , *J. Catal.* 378 (2019) 17–27.
- [30] M. Liu, J. Lee, T.-C. Yang, F. Zheng, J. Zhao, C.-M. Yang, L.Y.S. Lee, Synergies of Fe single atoms and clusters on N-doped carbon electrocatalyst for pH-universal oxygen reduction, *Small Methods* 5 (5) (2021) 2001165.
- [31] Y. Shang, X. Xu, B. Gao, S. Wang, X. Duan, Single-atom catalysis in advanced oxidation processes for environmental remediation, *Chem. Soc. Rev.* 50 (8) (2021) 5281–5322.
- [32] J. Tang, J. Wang, Metal organic framework with coordinatively unsaturated sites as efficient Fenton-like catalyst for enhanced degradation of sulfamethazine, *Environ. Sci. Technol.* 52 (9) (2018) 5367–5377.
- [33] S. Li, X. Zhang, Y. Huang, Zeolitic imidazolate framework-8 derived nanoporous carbon as an effective and recyclable adsorbent for removal of ciprofloxacin antibiotics from water, *J. Hazard. Mater.* 321 (2017) 711–719.
- [34] Y. Zhang, Y. Li, J. Chen, P. Zhao, D. Li, J. Mu, L. Zhang, $\text{CoO}/\text{Co}_3\text{O}_4/\text{graphene}$ nanocomposites as anode materials for lithium-ion batteries, *J. Alloy. Compd.* 699 (2017) 672–678.
- [35] W.-D. Oh, S.-K. Lua, Z. Dong, T.-T. Lim, High surface area DPA-hematite for efficient detoxification of bisphenol A via peroxymonosulfate activation, *J. Mater. Chem. A* 2 (38) (2014) 15836–15845.
- [36] W. Liu, W. Hu, L. Yang, J. Liu, Single cobalt atom anchored on carbon nitride with well-defined active sites for photo-enzyme catalysis, *Nano Energy* 73 (2020) 104750.
- [37] J. Qiu, J. Hu, J. Lan, L. Wang, G. Fu, R. Xiao, B. Ge, J. Jiang, Pure siliceous zeolite-supported Ru single-atom active sites for ammonia synthesis, *Chem. Mater.* 31 (2019) 9413–9421.
- [38] W. Sun, Y. Xiao, Q. Ren, F. Yang, Soybean-waste-derived activated porous carbons for electrochemical-double-layer supercapacitors: effects of processing parameters, *J. Energy Storage* 27 (2020) 101070.
- [39] Y. Toyama, K. Miyake, Y. Shu, K. Moroto, J. Ma, T. Zheng, S. Tanaka, N. Nishiyama, C. Fukuhara, C.Y. Kong, Solvent-free synthesis of Fe/N doped hierarchical porous carbon as an ideal electrocatalyst for oxygen reduction reaction, *Mater. Today. Energy* 17 (2020) 100444.
- [40] Y. Yao, Y.i. Hu, H. Hu, L. Chen, M. Yu, M. Gao, S. Wang, Metal-free catalysts of graphitic carbon nitride-covalent organic frameworks for efficient pollutant destruction in water, *J. Colloid Interf. Sci.* 554 (2019) 376–387.
- [41] Y. Liu, T. Gan, Q. He, H. Zhang, X. He, H. Ji, Catalytic oxidation of 5-hydroxymethylfurfural to 2,5-diformylfuran over atomically dispersed ruthenium catalysts, *Ind. Eng. Chem. Res.* 59 (10) (2020) 4333–4337.
- [42] T. Gan, Y. Liu, Q. He, H. Zhang, X. He, H. Ji, Facile synthesis of kilogram-scale alloyed Pt single-atom catalysts via ball milling for hydrodeoxygenation of 5-hydroxymethylfurfural, *ACS Sustain. Chem. Eng.* 8 (23) (2020) 8692–8699.
- [43] T. Gan, Q. He, H. Zhang, H. Xiao, Y. Liu, Y. Zhang, X. He, H. Ji, Unveiling the kilogram-scale gold single-atom catalysts via ball milling for preferential oxidation of CO in excess hydrogen, *Chem. Eng. J.* 389 (2020) 124490.
- [44] C. Feng, Y. Guo, S. Qiao, Y. Xie, L.i. Zhang, L. Zhang, W. Wang, J. Wang, 2-Methylimidazole as a nitrogen source assisted synthesis of a nano-rod-shaped Fe/FeN@N-C catalyst with plentiful FeN active sites and enhanced ORR activity, *Appl. Surf. Sci.* 533 (2020) 147481.
- [45] H.e. Miao, S. Li, Z. Wang, S. Sun, M. Kuang, Z. Liu, J. Yuan, Enhancing the pyridinic N content of nitrogen-doped graphene and improving its catalytic activity for oxygen reduction reaction, *Int. J. Hydrogen Energ.* 42 (47) (2017) 28298–28308.
- [46] Y. Xu, Y. Mo, J. Tian, P. Wang, H. Yu, J. Yu, The synergistic effect of graphitic N and pyrrolic N for the enhanced photocatalytic performance of nitrogen-doped graphene/ TiO_2 nanocomposites, *Appl. Catal. B-Environ.* 181 (2016) 810–817.
- [47] M.E.M. Buan, A. Cognigni, J.C. Walmsley, N. Muthuswamy, M. Ronning, Active sites for the oxygen reduction reaction in nitrogen-doped carbon nanofibers, *Catal. Today* 357 (2020) 248–258.
- [48] K. Mamtani, D. Jain, D. Zemlyanov, G. Celik, J. Luthman, G. Renkes, A.C. Co, U. S. Ozkan, Probing the oxygen reduction reaction active sites over Nitrogen-doped carbon nanostructures (CN_x) in acidic media using phosphate anion, *ACS Catal.* 6 (10) (2016) 7249–7259.
- [49] T. Zang, H. Wang, Y. Liu, L.i. Dai, S. Zhou, S. Ai, Fe-doped biochar derived from waste sludge for degradation of rhodamine B via enhancing activation of peroxymonosulfate, *Chemosphere* 261 (2020) 127616.
- [50] X. Liu, X. Zhang, K. Zhang, C. Qi, Sodium persulfate-assisted mechanochemical degradation of tetrabromobisphenol A: Efficacy, products and pathway, *Chemosphere* 150 (2016) 551–558.
- [51] P. Xin, J. Li, Y.u. Xiong, X.i. Wu, J. Dong, W. Chen, Y.u. Wang, L. Gu, J. Luo, H. Rong, C. Chen, Q. Peng, D. Wang, Y. Li, Revealing the active species for aerobic alcohol oxidation by using uniform supported palladium catalysts, *Angew. Chem. Int. Ed.* 57 (17) (2018) 4642–4646.
- [52] L. Zhang, R. Si, H. Liu, N. Chen, Q. Wang, K. Adair, Z. Wang, J. Chen, Z. Song, J. Li, M.N. Banis, R. Li, T. Sham, M. Gu, L. Liu, G.A. Botton, X. Sun, Atomic layer deposited Pt-Ru dual-metal dimers and identifying their active sites for hydrogen evolution reaction, *Nat. Commun.* 10 (2019) 4936.
- [53] H. Wang, W. Guo, B. Liu, Q. Si, H. Luo, Q. Zhao, N. Ren, Sludge-derived biochar as efficient persulfate activators: Sulfurization-induced electronic structure modulation and disparate nonradical mechanisms, *Appl. Catal. B-Environ.* 279 (2020) 119361.
- [54] J. Lee, U. von Gunten, J. Kim, Persulfate-based advanced oxidation: critical assessment of opportunities and roadblocks, *Environ. Sci. Technol.* 54 (2020) 3064–3081.
- [55] T. Rasheed, M. Bilal, H.M.N. Iqbal, S.Z.H. Shah, H. Hu, X. Zhang, Y. Zhou, TiO_2/UV -assisted rhodamine B degradation: putative pathway and identification of intermediates by UPLC/MS, *Environ. Technol.* 39 (2018) 1533–1543.
- [56] W. Ren, C. Cheng, P. Shao, X. Luo, H. Zhang, S. Wang, X. Duan, Origins of electron-transfer regime in persulfate-based nonradical oxidation processes, *Environ. Sci. Technol.* 56 (1) (2022) 78–97.
- [57] F. Sabatini, R. Giugliano, I. Degano, Photo-oxidation processes of Rhodamine B: a chromatographic and mass spectrometric approach, *Microchem. J.* 140 (2018) 114–122.
- [58] Z. He, C. Sun, S. Yang, Y. Ding, H. He, Z. Wang, Photocatalytic degradation of Rhodamine B by Bi_2WO_6 with electron accepting agent under microwave irradiation: mechanism and pathway, *J. Hazard. Mater.* 162 (2-3) (2009) 1477–1486.
- [59] G. Sharma, D.D. Dionysiou, S. Sharma, A. Kumar, A.H. Al-Muhtaseb, M. u. Naushad, F.J. Stadler, Highly efficient Sr/Ce/activated carbon bimetallic nanocomposite for photoinduced degradation of rhodamine B, *Catal. Today* 335 (2019) 437–451.